Electrochemical Reduction and Reoxidation Accompanied by Reversible Geometric Isomerization. Electrochemistry of $[Rh(\mu\text{-}t\text{-}Bu_2P)(CO)_2]_2$. Isolation and X-ray Crystal Structure of $[N(n\text{-}Bu)_4]_2^+[Rh(\mu\text{-}t\text{-}Bu_2P)(CO)_2]_2^{2-}$

John G. Gaudiello, Thomas C. Wright, Richard A. Jones,* and Allen J. Bard*

Contribution from the Department of Chemistry, The University of Texas at Austin, Austin, Texas 78712. *Received May 9, 1984*

Abstract: Electrochemical studies on $[Rh(\mu\text{-}t\text{-}Bu_2P)(CO)_2]_2$ have shown that upon reduction in THF it undergoes an ECE-type mechanism, a chemical reaction coupled between two electron-transfer reactions, to form a dianion. The chemical step is a geometric isomerization, producing an isomer which is more easily reduced than the parent compound. Oxidation of the dianion back to the neutral compound occurs by two one-electron oxidations followed by the reverse isomerization. Spectroscopic and crystallographic data, as well as digital simulations of the voltammetric responses, are presented to support the proposed mechanism. The dianion, $[Rh(\mu\text{-}t\text{-}Bu_2P)(CO)_2]_2^{2-}$, was isolated as the $N(n\text{-}Bu)_4^+$ salt, and its structure in the solid state has been determined by a single-crystal X-ray diffraction study. The two Rh atoms of the dianion have pseudotetrahedral geometries and a Rh–Rh distance of 2.840 (1) Å which is consistent with a metal–metal bond of order one. Crystal data: $C_{52}H_{108}N_2O_4P_2Rh_2$, M = 1093.22, monoclinic, $P2_1/c$, a = 14.138 (1) Å, b = 14.370 (4) Å, c = 21.127 (1) Å, β = 107.367 (3)°, U = 4096.8 (1) Å^3, D_c = 1.688 g cm^{-3}, Z = 2, λ(Mo Kα) = 0.71069 Å, μ(Mo Kα) = 9.27 cm^{-1}, final R = 0.0688, R_w = 0.0945 from 2729 observed reflections ($I > 2\sigma(I)$), 4463 measured.

Geometric rearrangement or isomerization upon either oxidation or reduction has been observed for a number of organic and inorganic systems. Previous studies from this laboratory and others have shown that organic molecules containing either steric strain or activated functionalities may rearrange following electron transfer.[1] Bond, Geiger, and others have observed similar effects with organometallic complexes, especially those containing diphenylphosphido ligands.[2]

There is currently considerable interest in the chemistry of phosphido- and arsenido-bridged complexes of the transition metals.[3] As part of a broad program designed to study the steric and electronic effects of phosphido complexes, we have investigated the use of sterically demanding (bulky) alkyl groups attached to phosphorus[4-13] or arsenic.[14] Our initial studies have focused on the use of the di-*tert*-butylphosphido group ($t\text{-}Bu_2P^-$).

For rhodium a number of phosphido-bridged complexes have been reported.[15] We recently described the unusual dinuclear Rh(I) system based on two isomers of the di-*tert*-butylphosphido-bridged complex $[Rh(\mu\text{-}t\text{-}Bu_2P)(CO)_2]_2$ (see Scheme I). The interesting feature of this system is a facile reversible metal–metal bond cleavage accompanied only by a geometric isomerization. We have noted that for dinuclear phosphido-bridged complexes of the Co group with roughly planar M_2P_2 central cores, three geometric isomers have been observed—A, B, and C (see Scheme II).[8,9,11] On the basis of bond length considerations, the geometry about each metal atom (either tetrahedral or planar) may be correlated with metal–metal bonds of order 0, 1, and 2 in A, B, and C, respectively. By reaction with PMe_3, isomers **1** and **2** may be converted into complex **3**, con-

(1) (a) Yeh, L.-S. R.; Bard, A. J. *J. Electrochem. Soc.* **1973**, *124*, 189–195. (b) Bard, A. J.; Puglisi, V. J.; Kenkel, J. V.; Lomax, A. *Discuss. Faraday Soc.* **1973**, *56*, 353–366. (c) Yeh, L.-S. R.; Bard, A. J. *J. Electroanal. Chem.* **1976**, *70*, 157–169. (d) Phelps, J.; Bard, A. J. *Ibid.* **1976**, *68*, 313–335. (e) Yeh, L.-S. R.; Bard, A. J. *Ibid.* **1977**, *81*, 333–338. (f) Chien, C. K.; Wang, H. C.; Szwarz, M.; Bard, A. J.; Itaya, K. *J. Am. Chem. Soc.* **1980**, *102*, 3100–3104. (g) Olsen, B. A.; Evans, D. H. *Ibid.* **1981**, *103*, 839–843. (h) Ahlberg, E.; Hammerich, O.; Parker, V. D. *Ibid.* **1981**, *103*, 844–849. (i) Neta, P.; Evans, D. H. *Ibid.* **1981**, *103*, 7041–7045. (j) Evans, D. H.; Busch, R. W. *Ibid.* **1982**, *104*, 5057–5062. (k) Olsen, B. A.; Evans, D. H.; Agranat, I. *J. Electroanal. Chem.* **1982**, *136*, 139–148. (l) Evans, D. H.; Xie, N. *J. Am. Chem. Soc.* **1983**, *105*, 315–320.

(2) (a) Wimmer, F. L.; Snow, M. R.; Bond, A. M. *Inorg. Chem.* **1974**, *13*, 1617–1623. (b) Bond, A. M.; Colton, R.; Jackowski, J. J. *Ibid.* **1975**, *14*, 274–278. (c) Bond, A. M.; Colton, R.; McCormick, M. J. *Ibid.* **1977**, *16*, 155–159. (d) Bond, A. M.; Grabaric, B. S.; Grabaric, Z. *Ibid.* **1978**, *17*, 1013–1018. (e) Bond, A. M.; Colton, R.; Jackowski, J. J. *Ibid.* **1978**, *17*, 2153–2160. (f) Bond, A. M.; Colton, R.; McDonald, M. E. *Ibid.* **1978**, *17*, 2842–2847. (g) Bond, A. M.; Keene, F. R.; Rumble, N. W.; Searle, G. H.; Snow, M. R. *Ibid.* **1978**, *17*, 2847–2853. (h) Bond, A. M.; Darensbourg, D. J.; Mocellin, E.; Stewart, B. J. *Ibid.* **1981**, *19*, 6737–6732. (i) Takvoryan, K.; Katovic, V.; Lovecchio, F. L.; Gore, E. S.; Anderson, L. B.; Busch, D. H. *J. Am. Chem. Soc.* **1974**, *96*, 731–742. (j) Holloway, J.; Bowden, W.; Geiger, W. E. *Ibid.* **1977**, *99*, 7089–7090. (k) Holloway, J.; Geiger, W. E. *Ibid.* **1979**, *101*, 2038–2044. (l) Moraczewski, J.; Geiger, W. E. *Ibid.* **1979**, *101*, 3407–3408. (m) Tulyathan, B.; Geiger, W. E. *Ibid.* **1980**, *109*, 325–331. (n) Moraczewski, J.; Geiger, W. E. *J. Am. Chem. Soc.* **1981**, *103*, 4779–4787. (o) Albright, T. A.; Geiger, W. E.; Moraczewski, J.; Tulyathan, B. *Ibid.* **1981**, *103*, 4787–4794. (p) Arewgoda, C. M.; Robinson, B, H.; Simpson, J. *J. Chem. Soc., Chem. Commun.* **1982**, *92*, 284–285.

(3) For leading references see: (a) Breen, M. J.; Geoffroy, G. L.; Rheingold, A. L *J. Am. Chem. Soc.* **1983**, *105*, 1069–1070. (b) Fultz, W. C.; Rheingold, A. L.; Kreter, P. E.; Meek, D. W. *Inorg. Chem.* **1983**, *22*, 860–863. (c) Carty, A. J. *Adv. Chem. Ser.* **1982**, *No. 196*, 163. (d) Braunstein, P.; Mott, D.; Fars, O.; Louer, M.; Grandjean, D.; Fischer, J.; Mitschler, A. *J. Organomet. Chem.* **1981**, *213*, 79–92. (e) Yu, Y.-F.; Gallucci, J.; Wojcicki, A. *J. Am. Chem. Soc.* **1983**, *105*, 4826–4828. (f) Zolk, R.; Werner, H. *J. Organomet. Chem.* **1983**, *252*, C53–C56. (g) Müller, M.; Vahrenkamp, H. *Chem. Ber.* **1983**, *116*, 2322–2336.

(4) Jones, R. A.; Stuart, A. L.; Atwood, J. L.; Hunter, W. E.; Rogers, R. D. *Organometallics* **1982**, *1*, 1721–1723.

(5) Jones, R. A.; Wright, T. C.; Atwood, J. L.; Hunter, W. E. *Inorg. Chem.* **1983**, *22*, 993–995.

(6) Jones, R. A.; Wright, T. C.; Atwood, J. L.; Hunter, W. E. *Organometallics* **1983**, *2*, 470–472.

(7) Jones, R. A.; Stuart, A. L.; Atwood, J. L.; Hunter, W. E. *Organometallics* **1983**, *2*, 874–878.

(8) Jones, R. A.; Stuart, A. L.; Atwood, J. L.; Hunter, W. E. *Organometallics* **1983**, *2*, 1437–1441.

(9) Jones, R. A.; Norman, N. C.; Seeberger, M. H.; Atwood, J. L.; Hunter, W. E. *Organometallics* **1983**, *2*, 1629–1634.

(10) Jones, R. A.; Lasch, J. G.; Norman, N. C.; Wright, T. C. *J. Am. Chem. Soc.* **1983**, *105*, 6184.

(11) Jones, R. A.; Wright, T. C. *Organometallics* **1983**, *2*, 1842–1845.

(12) Jones, R. A.; Lasch, J. G.; Norman, N. C.; Stuart, A. L.; Wright, T. C.; Whittlesey, B. R. *Organometallics* **1984**, *3*, 114–119.

(13) Jones, R. A.; Stuart, A. L.; Wright, T. C. *J. Am. Chem. Soc.* **1983**, *105*, 7459–7460.

(14) Jones, R. A.; Whittlesey, B. R. *Organometallics* **1984**, *3*, 469–475.

(15) (a) Jamerson, J. D.; Pruett, R. L.; Billig, E.; Fiato, F. A. *J. Organomet. Chem.* **1980**, *193*, C43–C46. (b) Billig, E.; Jamerson, J. D.; Pruett, R. L.; *Ibid.* **1980**, *192*, C49–C51. (c) Haines, R. J.; Steen N. D. C. T.; English, R. B. *Ibid.* **1981**, *209*, C34–C36. (d) Kreter, P. E.; Meek, D. W.; Christoph, G. G. *Ibid.* **1980**, *188*, C27–C30. (e) Meek, D. W.; Kreter, P. E.; Christoph, G. G. *Ibid.* **1982**, *231*, C53–C55. (f) Kreter, P. E.; Meek, D. W. *Inorg. Chem.* **1983**, *22*, 319–326. (g) Burkhardt, E. W.; Mercer, W. C.; Geoffroy, G. L.; Rheingold, A. L.; Fultz, W. C. *J. Chem. Soc., Chem. Commun.* **1983**, 1251–1252.

0002-7863/85/1507-0888$01.50/0

Scheme I

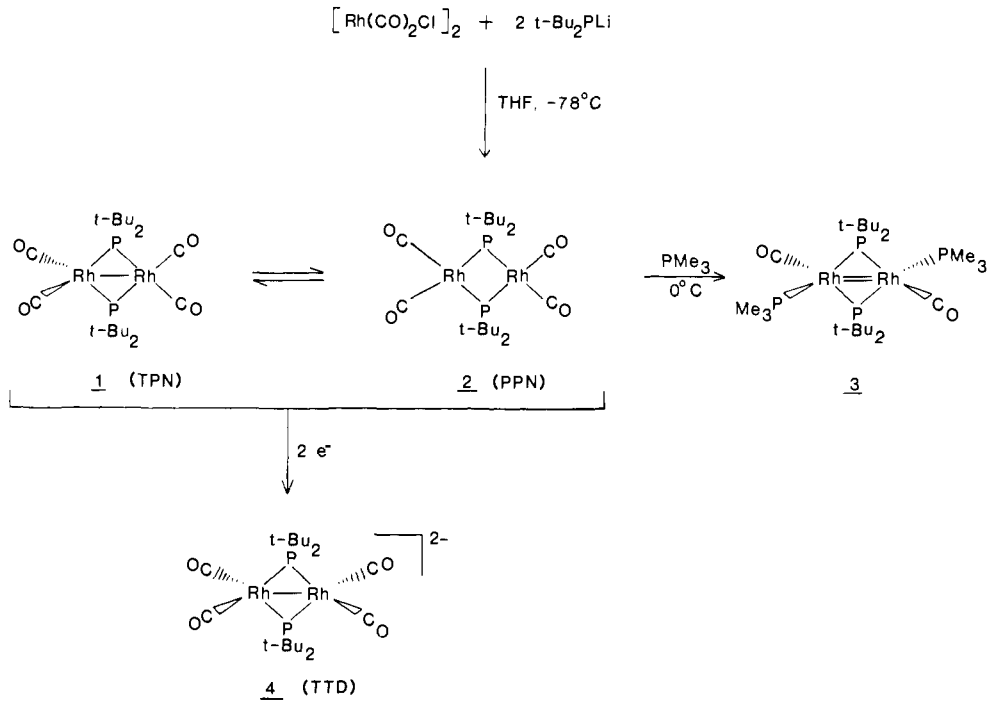

Scheme II

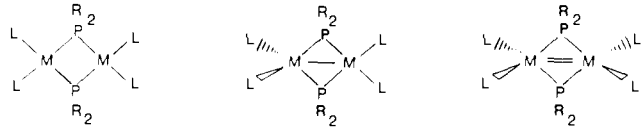

M = Co, Rh, Ir

L = 2 electron donor (CO, PR_3, N_2, etc.)

taining a Rh–Rh double bond. Relief of steric strain is thought to be largely responsible for the adoption of roughly tetrahedral geometries for the Rh atoms in **3**.[11]

The electrochemistry of phosphorus- and arsenic-bridged metal carbonyl complexes containing a metal–metal bond was initially investigated by Dessy and co-workers.[16] These complexes all exhibited a single two-electron polarographic reduction wave. Although the presence of the one-electron intermediate, the anion, was not observed by electrochemical means, mixing the dianion and neutral complex resulted in the formation of an anion displaying an ESR signal.[17] Collman et al. have recently described the electrochemistry of $[Fe(\mu\text{-}Ph_2P)(CO)_3]_2$, which also undergoes a single two-electron reduction.[18] However, mixtures of the dianion and neutral complex did not produce an anion. The dianion was found to have a planar Fe_2P_2 skeleton and no Fe–Fe bond.

We show here that the Rh(I) system (Schemes III and IV) isomerizes upon both electrochemical reduction and reoxidation. Reduction to a dianion occurs by two successive one-electron reductions with an intervening geometric isomerization. The second electron transfer is thermodynamically easier than the first. Surprisingly, the oxidation of the dianion back to the starting material occurs by two one-electron oxidations followed by the reverse geometric isomerization. The dianion is unusual in that it still contains a metal–metal bond. The behavior is believed to be due to a number of competing electronic and steric factors.

This paper describes our electrochemical studies including digital simulations of the voltammetric responses in support of the proposed mechanism, as well as the spectroscopic characterization and X-ray crystal structure of the dianion $[Rh(\mu\text{-}t\text{-}Bu_2P)(CO)_2]_2^{2-}$ as its $n\text{-}Bu_4N^+$ salt.

Experimental Section

Chemicals. $[Rh(\mu\text{-}t\text{-}Bu_2P)(CO)_2]_2$ was prepared as previously described.[6] Tetra-*n*-butylammonium fluorobrate ($(TBA)BF_4$), used as supporting electrolyte, was obtained from Southwestern Analytical Chemicals (Austin, TX) and recrystallized three times from acetone/ether. THF (MCB) was dried and degassed by distillation from potassium benzophenone ketyl under nitrogen and then freeze–pump–thawed five times. The solvent was stored under helium in a drybox (Vaccum Atmospheres, Hawthorne, CA).

Measurements. Electrochemical measurements were performed with a Princeton Applied Research (PAR) Model 175 universal programmer, a PAR Model 173 potentiostat, and a Model 179 digital coulometer (Princeton Applied Research Corp., Princeton, NJ). Positive feedback was used to compensate for *iR* drop. A Model 2000 *X–Y* recorder (Houston Instruments, Inc., Austin, TX) was used to record the cyclic voltammograms for scan rates less than 500 mV s^{-1}. Scan rates greater than 500 mV s^{-1} were recorded with a Model 3001 Processing Oscilloscope (Norland Corp., Fort Atkinson, WI). Measurements were made in the three-electrode configuration with a platinum disk working electrode (area, 0.030 cm^2), a platinum gauze auxiliary electrode, and a silver wire quasi-reference electrode. The potential of the reference electrode was determined to be ca. −0.36 V vs. SCE by using the ferrocene/ferrocenium couple as an internal standard. A small amount of ferrocene was added at the end of each experiment.

Electrochemical studies were carried out in one- and three-compartment cells with all connections made through ground glass joints.[19] The solutions and cells were prepared and sealed inside the drybox prior to removal for study.

Samples for NMR and IR analysis were prepared electrochemically in THF (0.5 M $(TBA)BF_4$) and then transferred by standard Schlenk-line techniques. $^{31}P\{^1H\}$ NMR spectra were obtained on a Varian FT-80 (32.384 MHz) instrument and are referenced to external 85% H_3PO_4 (δ 0.0). $^{13}C\{^1H\}$ NMR spectra (^{13}CO enriched) were obtained on a Bruker WH-90 (22.615 MHz) instrument and are referenced to external Me_4Si (δ 0.0). IR spectra were recorded on a Perkin-Elmer 1330 spectrometer with matched KBr cells (THF solution).

Characterization of $(n\text{-}Bu_4N)_2[Rh(\mu\text{-}t\text{-}Bu_2P)(CO)_2]_2$ (4). The complex, generated electrochemically, can be crystallized from THF solutions (−40 °C): IR 1760 (s), 1733 cm^{-1} (s); $^{31}P\{^1H\}$ δ 377.1 (t, $^1J_{Rh-P}$ = 117 Hz); $^{13}C\{^1H\}$ δ 218.0 (d, $^1J_{Rh-CO}$ = 83.9 Hz).

(16) Dessy R. E.; Kornmann, R.; Smith, C.; Hayter, R. *J. Am. Chem. Soc.* **1968**, *90*, 2001–2004.
(17) Dessy R. E.; Rheingold, A. L.; Howard, G. D. *J. Am. Chem. Soc.* **1972**, *94*, 746–752.
(18) Collman, J. P.; Rothrock, R. K.; Finke, R. G.; Moore, E. J.; Rose-Munch, F. *Inorg. Chem.* **1982**, *21*, 146–156.
(19) Smith, W. H.; Bard, A. J. *J. Am. Chem. Soc.* **1975**, *97*, 5203–5210.

Table I. Crystal Data and Summary of Intensity Data Collection and Structure Refinement of $[Rh(\mu\text{-}t\text{-}Bu_2P)(CO)_2]_2^{2-}$

formula	$C_{52}H_{108}N_2O_4P_2Rh_2$
mol wt	1093.2
space group	$P2_1/c$
cell constants	
a, Å	14.138 (1)
b, Å	14.370 (4)
c, Å	21.127 (1)
β, deg	107.367 (3)
cell vol, Å^3	4096.8 (1)
formula units/unit cell	2
D_{calcd}, g cm^{-3}	1.688
μ_{calcd}, cm^{-1}	9.27
radiation, Å	Mo Kα, 0.71069
max crystal dimensions, mm	0.15 × 0.19 × 0.20
scan width, deg	0.8 ± 0.35 tan θ
standard reflections	065, 535
decay of standards	<2%
reflections measured	4463
2θ range, deg	2–50
reflections obsd	2729 ($I > 2\sigma(I)$)
no. of parameters varied	280
data/parameter ratio	9.746
R	0.0688
R_w	0.0945

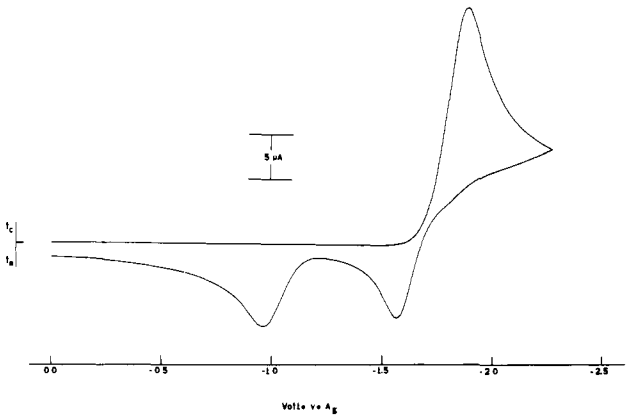

Figure 1. Cyclic voltammogram of 3.71 mM $[Rh(\mu\text{-}t\text{-}Bu_2P)(CO)_2]_2$ in THF/0.5 M $(TBA)BF_4$ scanned between 0.00 and −2.25 V. Scan rate 200 mV s^{-1}.

Digital Simulations. The simulated cyclic voltammograms are based on the explicit-finite-difference method.[20] The surface boundary conditions used for the E_iE_r case were the same as those employed by Feldberg for multiple electron-transfer reactions.[21] The equations for the surface conditions used in the ECE simulations are derived in the Appendix. Since the rearrangement following the second oxidation is believed to be extremely fast, the anion was taken to be oxidized directly to the starting material in the simulations.

X-ray Data Collection and Structure Determination

Crystals of the dianion suitable for X-ray studies were grown from THF solutions at −40 °C (ca. 13 mM, 0.5 M $(TBA)BF_4$, by electrochemical generation). They were mounted in thin-walled glass capillaries under nitrogen. Final lattice parameters were determined from 25 high-angle reflections ($26.0 > 2\theta > 30.0$) carefully centered on an Enraf-Nonius CAD-4 diffractometer. Data were collected by the $\omega/2\theta$ scan technique at 23 ± 2 °C. Details of crystal data and a summary of intensity data collection parameters are given in Table I. Details of data collection procedures were similar to those outline in ref 11. The space group was determined uniquely by systematic absences as $P2_1/c$.

Data were corrected for Lorentz and polarization effects. No absorption correction was applied. The structure was solved by direct methods and successive difference Fourier maps with use of the Enraf-Nonius software package "SDP-PLUS" (B. A. Frenz and Associates, College Station, TX 77840, 4th ed., 1981) on a PDP 11/44 computer. Scattering factors were taken from ref 22, and a non-Poisson weighting scheme was used. Hydrogen atoms were not located. The final full-matrix least-squares refinement with anisotropic thermal parameters gave final values of $R = 0.0688$ and $R_w = 0.0945$ ($R = \sum||F_o| - |F_c||/\sum|F_o|$ and $R_w = [\sum_\omega(|F_o| - |F_c|)^2/\sum_\omega(|F_o|)^2]^{1/2}$). The final difference Fourier map showed no chemically significant peaks with the highest peak being 0.5 e/Å^3 associated with the Rh atom.

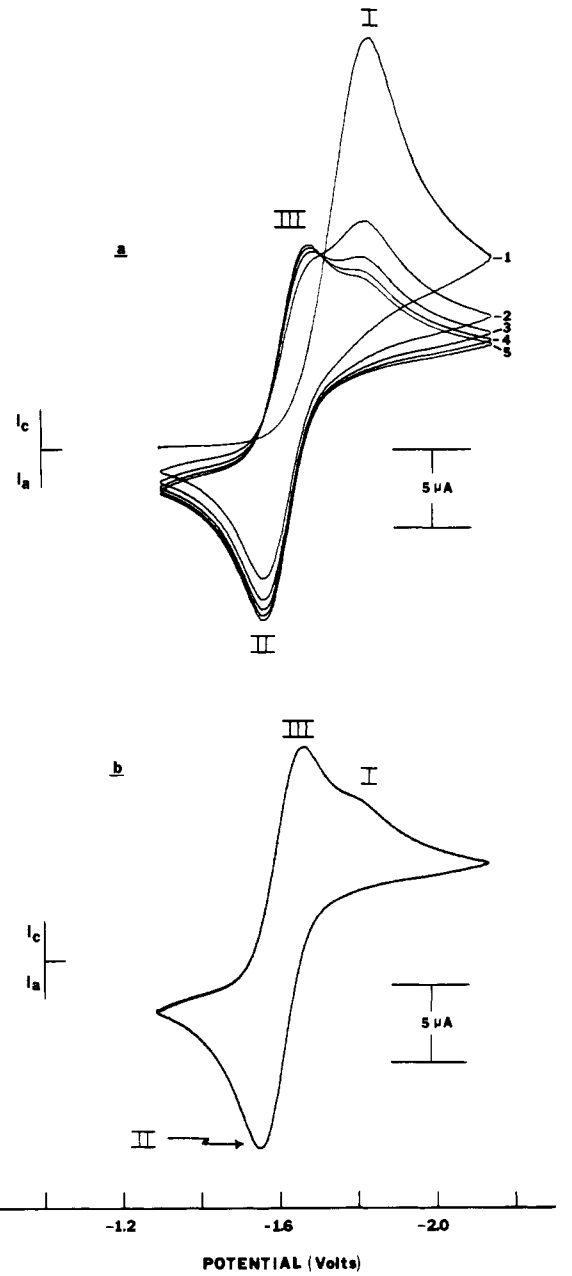

Figure 2. Cyclic voltammograms of 3.71 mM $[Rh(\mu\text{-}t\text{-}Bu_2P)(CO)_2]_2$ in THF/0.5 M $(TBA)BF_4$ scanned between −1.29 and −2.15 V. Scan rate 200 mV s^{-1}. (a) First five scans; (b) steady state observed after ca. 10 scans.

Results and Discussion

Electrochemical Studies. A typical cyclic voltammogram for the reduction of $[Rh(\mu\text{-}t\text{-}Bu_2P)(CO)_2]_2$ in THF at a Pt-disk electrode is shown in Figure 1. As will be shown in analysis of these voltammograms, the large reduction wave observed on the forward scan involves two one-electron reductions separated by a chemical step (i.e., an ECE mechanism). The chemical step

(20) (a) Feldberg, S. W. "Electroanalytical Chemistry"; Bard, A. J., Ed.; Dekker: New York, 1969; Vol. 3, p 199. (b) Bard, A. J.; Faulkner, L. R. "Electrochemical Methods"; John Wiley and Sons, Inc.: New York, 1980; Appdendix B.

(21) Feldberg, S. W. "Computer Applications in Analytical Chemistry"; Mark, H. B., Ed.; Dekker: New York, 1972; Chapter 7.

(22) "International Tables of Crystallography"; Kynoch Press: Birmingham, England, 1974; Vol. 4.

is believed to be a geometric isomerization producing an isomer which is more easily reduced than the parent compound. The reverse scan shows two smaller waves corresponding to two successive one-electron oxidations. The resulting neutral compound undergoes the reverse isomerization to regenerate the starting material.

Shown in Figure 2a are a series of successive cyclic voltammograms observed when the potential is scanned between −1.29 and −2.15 V. The first cathodic scan shows only a single large reduction wave (I), with a cathodic peak potential (E_{pc}) of −1.83 V. Upon scan reversal, a smaller oxidation wave (II) with an anodic peak potential (E_{pa}) of −1.56 V is observed. The second scan shows a new reduction wave, E_{pc} = −1.66 V, with the original wave (I, E_{pc} = −1.83 V) decreased in height. On the return scan, the oxidation wave at E_{pa} = −1.56 V is again observed. In subsequent scans the peak currents for waves II and III increased while the peak current for wave I decreased. In the steady-state voltammetric response observed after ca. 10 scans, wave I has almost disappeared (Figure 2b).

This type of behavior is characteristic of an ECE mechanism,[23] a chemical reaction coupled between two electron-transfer reactions, given schematically as

$$\text{"E"} \qquad A + e^- \rightleftarrows B \qquad E_1^\circ \qquad (1)$$

$$\text{"C"} \qquad B \xrightarrow{k_c} C \qquad (2)$$

$$\text{"E"} \qquad C + e^- \rightleftarrows D \qquad E_2^\circ \qquad (3)$$

where the reduction of C is thermodynamically more favorable than that of A ($E^\circ_{A/B} - E^\circ_{C/D} > 180$ mV). Wave I involves the reduction of A and C, producing D. Wave II corresponds to the oxidation of D to C and wave III to the reduction of C to D. Wave I as expected decreases in height with each successive scan since the surface concentration of A is decreasing. Simulations, described below, demonstrate that this mechanism is consistent with the observed voltammograms for the reduction of the Rh dimer.

Further evidence for this reaction path was obtained by bulk electrolysis controlled potential coulometry (CPC) experiments. CPC carried out at −2.20 V gave a dark red solution and an n_{app} value (Faradays per mole of reactant consumed) of 2.05. A voltammetric scan following this reduction starting at −2.2 V and sweeping toward positive potentials showed two oxidation waves, and on scan reversal a reduction wave in a voltammogram essentially the same as Figure 1 was shown. Oxidation of this solution at 0.0 V regenerated a solution which showed the identical cyclic voltammetric behavior as the original one. Oxidation of the solution prepared at −2.2 and −1.2 V with the passage of an amount of charge equivalent to $n_{app} = 1$ yielded a green solution. Examination of this solution by electron spin resonance showed a single peak with only slightly resolved splitting.

We now assign the waves to actual reactions of the compound. Wave I in Figure 2a is due to the initial one-electron reduction of the neutral tetrahedral/planar parent (TPN) followed by a fast chemical reaction to form a new electroactive species with an E° value less negative than that of TPN. Since the dianion (TTD) has a tetrahedral/tetrahedral geometry, both in the solid state and also in solution (see later), it seems reasonable to propose that the fast chemical reaction is a geometric isomerization of the tetrahedral/planar form of the anion (TPA) to a tetrahedral/tetrahedral one (TTA). The rate constant for the isomerization is at least 600 s^{-1}, since no peak corresponding ot the oxidation of TPA back to TPN was observed in the cyclic voltammograms upon potential scan reversal at scan rates as high as 200 V s^{-1}. The proposed transformations are outlined in Scheme III.

Since $E^\circ_{TTA/TTD} \gg E^\circ_{TPN/TPA}$, waves II and III in Figure 2a involve the anion/dianion couple (reaction 6). Both forms of the couple are stable on a voltammetric time scale, since no decay in the steady-state current was observed after ca. 10 min of continuous cycling. The steady-state voltammogram for the anion/dianion couple is characteristic of a reversible one-electron process. The anodic and cathodic peak currents, i_{pa} and i_{pc}, are equal, and the peak potentials, E_{pa} and E_{pc}, are essentially invariant for scan rates between 50 and 500 mV s^{-1}. Over this range of scan rates, the difference in the peak potentials ($\Delta E_p = E_{pa} - E_{pc}$) is 80 mV, which is slightly larger than the expected 58 mV for the one-electron Nernstian process.[24] This can be attributed to some uncompensated solution resistance in the THF medium. The ferrocene/ferrocenium couple, which shows rapid heterogeneous electron transfers in most solvents, also gave a ΔE_p of 80 mV. At higher scan rates, ΔE_p increases and is ~500 mV (reflecting increased uncompensated resistance effects as well as kinetic contributions) at 200 V s^{-1}.

The initial peak current for the reduction of the neutral compound (wave I, scan 1, Figure 2a) is approximately twice as large as the steady-state current for the TTA/TTD couple when measuring from the decaying base line (Figure 2b). This behavior is expected for an ECE mechanism only when (a) $E^\circ_{C/D} \gg E^\circ_{A/B}$; (b) the rate of the chemical reaction (reaction 2) is fast on the time scale of the experiment;[25] and (c) the same number of electrons are transferred in each step.[23] Wave I on the first scan is also more drawn out than the steady-state wave for the TTA/TTD couple. This behavior is characteristic of a totally irreversible electron-transfer reaction. For the reaction scheme shown above, two factors could lead to such behavior. First, the chemical reaction could be extremely fast. This would remove TPA before the back electron transfer could occur and shift the wave to less negative potentials. This shift causes a decrease in the rate of the first heterogeneous charge-transfer reaction (reaction 4), causing the wave to look irreversible, even though the standard heterogeneous rate constant (k°) is large. Alternatively, k° for the TPN/TPA couple could be small. We believe that the apparent irreversibility can be attributed to the following reaction being extremely fast, since k_c is at least 600 s^{-1}.

Additional evidence supporting an ECE mechanism is the occurrence of an isopotential point at −1.71 V (Figure 2a). An isopotential point (IPP), the electrochemical equivalent of an isosbestic point in spectroscopy, arises in voltammetry when one electroactive species undergoes a transformation to form another.[26] As will be discussed in more detail elsewhere, the existence of an IPP implies that the transformation is quantitative and the sum of the reactants and products remain constant. If there are any side reactions involving either set of species, an IPP will not occur. IPP's have been observed for materials confined to an electrode surface, polymer films, and adsorbed and electrodeposited species but to our knowledge never for a system where both the reactants and products are dissolved in solution. As will be shown via simulations, the isopotential point in Figure 2a can be traced to the isomerization of TPA to TTA, reaction 5.

When the potential is scanned between 0.00 and −2.25 V (Figure 1), the large reduction wave at E_{pc} = −1.83 V (TPN → TTD) and the first oxidation wave upon potential reversal, E_{pa} = −1.56 V (TTD → TTA), are again observed. (This behavior is identical with that observed when the potential was scanned between −1.29 and −2.15 V.) The second oxidation wave, E_{pc} = −0.93 V, is more drawn out than the first. The peak current, when measured from the decaying base line, is also smaller than the first. Like the large reduction wave in Figure 2a, this behavior is characteristic of a totally irreversible electron-transfer reaction. We believe that this irreversibility is again due to a fast following

(23) (a) Nicholson, R. S; Shain, I. *Anal. Chem.* **1965**, *37*, 178–190. (b) Saveant, J. M. *Electrochim. Actas* **1967**, *12*, 753–766.

(24) Nicholson, R. S.; Shain, I. *Anal. Chem.* **1964**, *36*, 706–723.

(25) The chemical rate constant, k_c, is usually normalized to the time scale of the experiment by defining a dimensionless homogeneous kinetic parameter λ. In cyclic voltammetry, for an ECE mechanism, $\lambda = k_c RT/nFv$ where R, T, n, and F have their usual significance and v is the scan rate in V s^{-1}.[23a] For λ > 5, the chemical reaction is fast on the time scale of the experiment and the peak current limits at a value controlled by $n_1 + n_2$, independent of λ.

(26) (a) Untereker, D. F.; Bruckenstein, S. *Anal. Chem.* **1972**, *44*, 1009–1020. (b) Cadle, S. H.; Bruckenstein, S. *Ibid.* **1972**, *44*, 1993–2001. (c) Untereker, D. F.; Brukenstein, S. *J. Electroanal. Chem.* **1974**, *57*, 77–87. (d) Cadle, S. H. *Anal. Chem.* **1974**, *46*, 587–592. (e) Abruna, H. D.; Walsh, J. L.; Meyer T. J.; Murray, R. W. *Inorg. Chem.* **1981**, *20*, 1418–1486. (f) Day, R. W.; Inzelt, G.; Kinstle. J. L.; Chambers, J. Q. *J. Am. Chem. Soc.* **1982**, *104*, 6804–6805.

Scheme III. Proposed Geometrical Isomerization Accompanying Electrochemical Reduction[a]

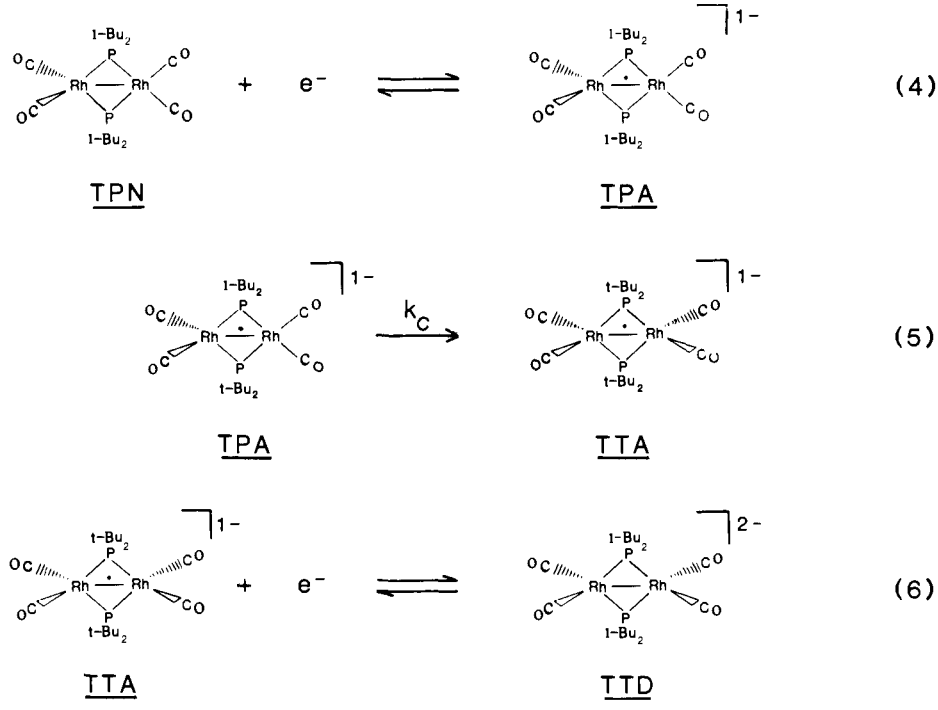

(4) (5) (6)

[a] The abbreviations for each species describe the approximate geometry of the metals (i.e., T = tetrahedral, P = planar) and the charge on the complex (N = neutral, A = anion, D = dianion).

Scheme IV. Proposed Geometrical Isomerization Accompanying Electrochemical Oxidation

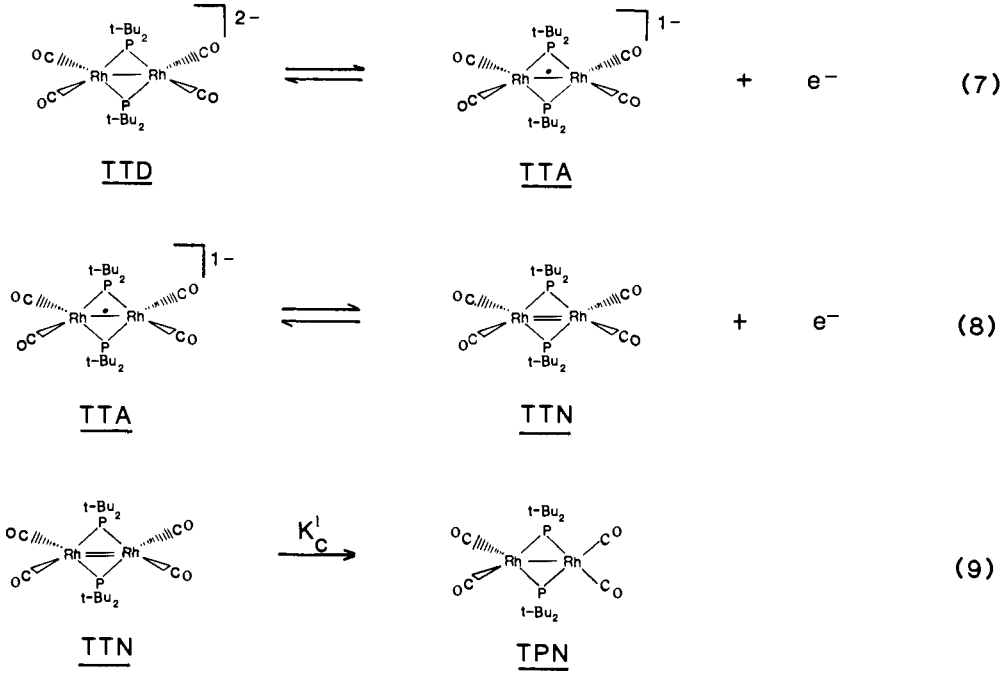

(7) (8) (9)

chemical reaction (TTN → TPN) and not to a small value for $k°$; i.e., the second oxidation wave is thus a one-electron oxidation of TTA to a tetrahedral/tetrahedral form of the neutral compound (TTN) which isomerizes rapidly to the starting material (TPN). The rate constant for the reaction is at least 600 s^{-1}, since no reduction peak is observed upon potential reversal at scan rates as high as 200 V s^{-1}. The reverse scan can be represented by the set of reactions outlined in Scheme IV.

After ca. five scans, the cyclic voltammograms achieved a steady-state response, indicating that the starting material is regenerated by the second oxidation. This supports the EEC-type mechanism shown in Scheme IV. A steady-state response would not be obtained if any of the above species were involved in a reaction to form a compound not included in the above reaction scheme (reactions 4–9). However, inclusion of a disproportionation step, for example, a reaction between TPN and TTD to give TPA and TTA, in the above scheme would also give a steady-state response. We show that this disproportionation reaction probably occurs. Similar cyclic voltammetric behavior has been observed by Evans and co-workers[1g,k] for bianthrone and substituted bianthrones, which show ECE/EEC-type mechanisms.

Digital simulations of the voltammograms were used to test the validity of the ECE model. To simulate these, the $E°$ values, the standard heterogeneous rate constants ($k_1°$ and $k_2°$), the chemical rate constant (k_c), and the diffusion coefficients must be assumed. $E_2°$ was taken as the average of E_{pc} and E_{pa} for the

TTA/TTD couple, −1.61 V. Values for $k°$ for both electron transfers were chosen to give a ΔE_p of 80 mV at 200 mV s^{-1}. This value was chosen to allow a close correspondence between the simulated and experimental voltammograms; as stated earlier, we believe the actual $k°$ values are much larger and the peak splittings observed are mainly caused by uncompensated resistance. The chemical rate constant was made sufficiently large (77.8 s^{-1}, λ = 10) that the peak current for the initial two-electron reduction wave was independent of k_c. $E_1°$ was set at −1.84 V, the value needed to make the peak potential for wave I occurs at −1.83 V when λ = 10. The diffusion coefficients, assumed equal for all species, were set at 1.7 × 10^{-6} cm^2 s^{-1}, the value obtained experimentally by chronoamperometry for TPN. Note that the various parameter values chosen for the simulation represent a representative, but not necessarily unique, set of values. For example, if k_c were larger, a different (more negative) value for $E°_1$ would be appropriate.

Figure 3a shows the simulated cyclic voltammograms for an ECE system with use of the parameters listed above. The scan rate and initial and switching potentials were the same as in Figure 2. The simulated results are similar to the experimental ones. As expected, the peak current for the initial reduction is approximately twice that of the C/D couple. The isopotential point at −1.74 V corresponds closely to the experimental value of −1.71 V. There are, however, a number of differences between the simulated and experimental results that could not be made smaller simply by variation of the input parameters. The peak current for the two-electron reduction (wave I) decays faster for each successive scan in the experimental voltammograms than in the simulated ones. The reduction wave for the C/D couple (wave III) is sharper and reaches a steady state faster in the experimental results. This suggests that a reaction other than the ones outlined in Schemes III and IV is also occurring. This reaction consumes A, causing wave I to decrease faster, and generates C, causing wave III to increase and reach a steady state sooner. A disproportionation reaction between A and D producing B and C would cause these effects.[27]

$$A + D \rightleftarrows B + C \tag{10}$$

Since B reacts quickly to form C, reaction 10 can be simplified to

$$A + D \rightleftarrows 2C \tag{11}$$

The equilibrium must lie to the right to account for the consumption of A and the generation of C. For the $[Rh(\mu\text{-}t\text{-}Bu_2P)(CO)_2]_2$ system, the disproportionation is between TPN and TTD giving two TTA (reaction 12).

$$TPN + TTD \underset{k_b}{\overset{k_f}{\rightleftharpoons}} 2TTA \tag{12}$$

When this reaction is included in the digital simulation, Figure 3b, excellent agreement with the experimental results is obtained. Values of 150 and 14.2 M^{-1} s^{-1} for k_f and k_b, respectively, gave the best fit.

Note that while the standard potentials for reactions 1 and 3 ($E_1°$ and $E_2°$) used in the simulations might seem to imply that the disproportionation reaction (reaction 10) would lie to the left, the fast following reaction (reaction 2) effectively drives the reaction in a direction shown. More specifically, if reaction 2 is considered to be a reversible one with a very large equilibrium constant (K), the $E°$ for the overall reaction A + e^- ⇄ C would be much less negative than $E°_1$ ($E°_{A/C} = E°_1 + 0.059 \log K$ at 25 °C), and this would cause reactions 11 and 12 to occur as shown.

The inclusion of the disproportionation reaction also accounts for the experimental observation that the first scan does not pass through the IPP (compare the simulations in Figure 3, a and b).

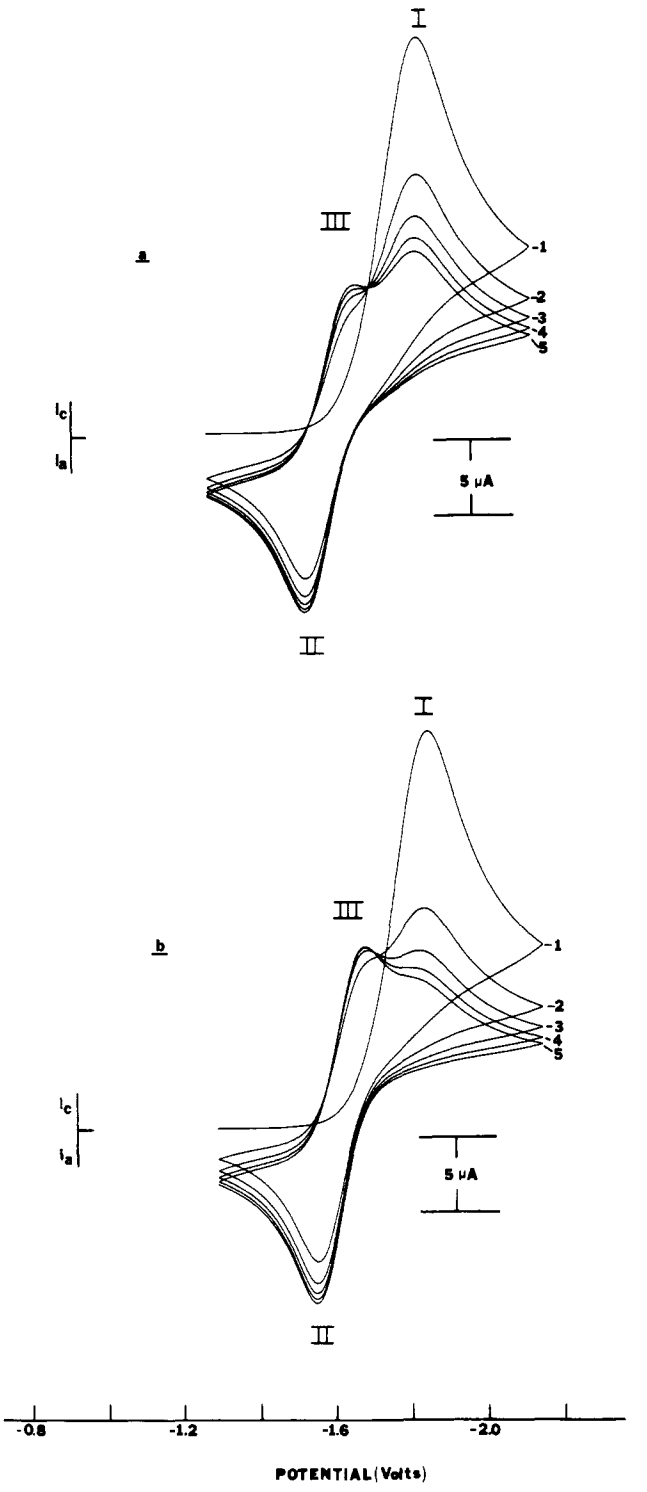

Figure 3. Simulated cyclic voltammograms based on C^* = 3.71 mM, D_0 = 1.7 × 10^{-6} cm^2 s^{-1}, $E°_1$ = −1.83 V, $E°_2$ = −1.61 V, $k°_1$ = 3.2 × 10^{-3} cm s^{-1}, $k°_2$ = 3.2 × 10^{-3} cm s^{-1}, α_1 = 0.5, α_2 = 0.5, k_c = 77.8 s^{-1} (λ = 10), k_f = 150 M^{-1} s^{-1}, k_b = 14.2 M^{-1} s^{-1}. Scan rate and initial and switching potentials are the same as in Figure 2: (a) ECE mechanism; (b) ECE-Disp mechanism.

Digital simulations covering the entire potential range, 0.00 to −2.25 V, were also run. Since the fast following chemical reaction (isomerization) makes the second oxidation electrochemically irreversible, TTA can be taken as oxidized directly to TPN.

$$TTA \rightarrow TPN + e^- \tag{13}$$

Figure 4 is a simulated cyclic voltammogram over the entire potential range for a ECE/EEC-Disp scheme (reactions 4–7, 13,

(27) (a) Hawley M. D.; Feldberg, S. W. *J. Phys. Chem.* **1966**, *70*, 3459–3463. (b) Amatore, C.; Gareil, M.; Saveant, J. M. *J. Electroanal. Chem.* **1983**, *147*, 1–38 and references therein.

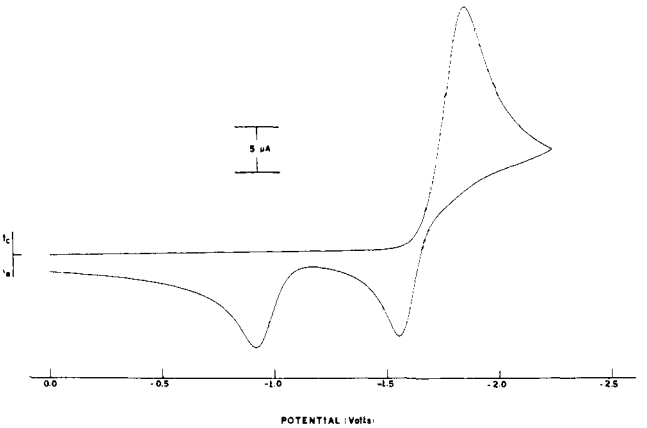

Figure 4. Simulated cyclic voltammograms for an ECE/EEC-Disp mechanism based on $E^\circ_3 = -1.24$ V, $k^\circ_3 = 1.6 \times 10^{-3}$ cm s^{-1}, $\alpha_3 = 0.65$, and the parameters listed for Figure 3. Scan rate and initial and switching potentials are the same as those listed for Figure 1.

and 12). This agrees well with the experimental voltammogram in Figure 1.

Table II. Positional Parameters and Their Estimated Standard Deviations[a]

atom	x	y	z	B, Å^2
Rh	0.46759 (7)	0.04949 (6)	0.04801 (1)	5.34 (2)
P(1)	0.3784 (2)	-0.0570 (2)	-0.0306 (4)	5.64 (8)
OO(1)	0.4904 (8)	-0.0091 (6)	0.1895 (4)	9.1 (3)
OO(2)	0.3684 (8)	0.2362 (6)	0.0240 (5)	10.3 (3)
CO(1)	0.487 (1)	0.0047 (9)	0.1353 (7)	7.1 (4)
CO(2)	0.408 (1)	0.1661 (8)	0.0267 (7)	7.2 (4)
C(1)	0.264 (1)	-0.0132 (9)	-0.0944 (6)	7.1 (4)
C(2)	0.341 (1)	-0.1732 (9)	-0.0009 (6)	7.5 (4)

[a] Anisotropically refined atoms are given in the form of the isotropic equivalent thermal parameter defined as $^4/_3[a^2B(1,1) + b^2B(2,2) + c^2B(3,3) + ab(\cos\gamma)B(1,2) + c(\cos\beta)B(1,3) + bc(\cos\alpha)B(2,3)]$.

Although the ECE-Disp mechanism fits the experimental results very well, an alternative model, involving slow heterogeneous electron transfers, is also possible. In this case the first electron transfer (TPN → TTA in one step) is slow and the second, which occurs at more negative potentials (TTA ⇄ TTD), is taken as rapid. Under these conditions the $E_rC_iE_r$ sequence becomes indistinguishable from an E_iE_r mechanism (an irreversible electron transfer followed by a reversible one). Simulated voltammograms,

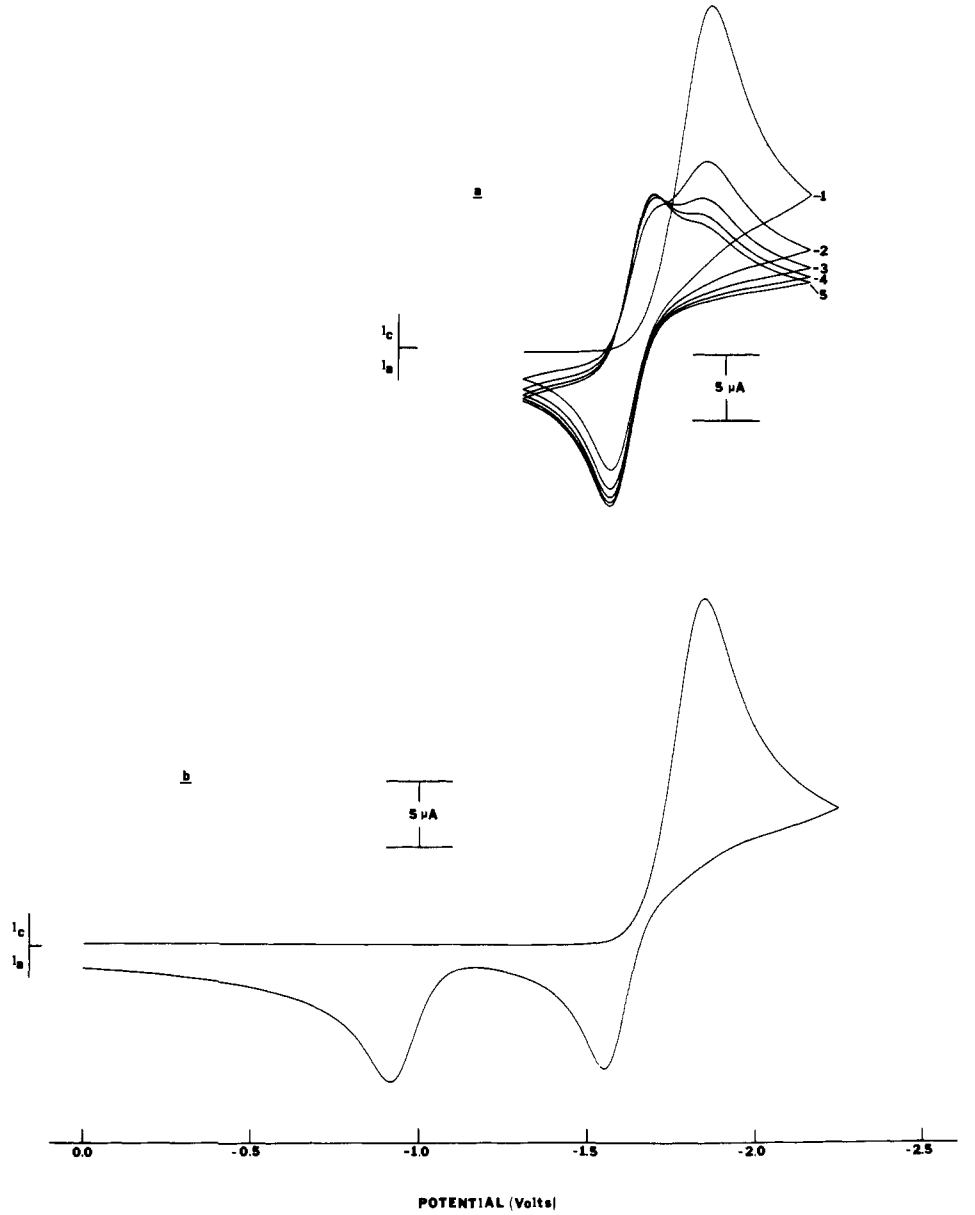

Figure 5. Simulated cyclic voltammograms for an E_iE_r-Disp mechanism based on $C^* = 3.71$ mM, $D_0 = 1.7 \times 10^{-6}$, $E^\circ_1 = -1.34$ V, $E^\circ_2 = -1.61$ V, $k^\circ_1 = 9.61 \times 10^{-7}$ cm s^{-1}, $k^\circ_2 = 3.2 \times 10^{-3}$ cm s^{-1}, $\alpha_1 = 0.45$, $\alpha_2 = 0.50$, $k_f = 150$ M^{-1} s^{-1}, $k_b = 14.2$ M^{-1} s^{-1}. Scan rate 200 mV s^{-1}. (a) Scanned between -1.29 and -2.15 V; (b) scanned between 0.00 and -2.25 V.

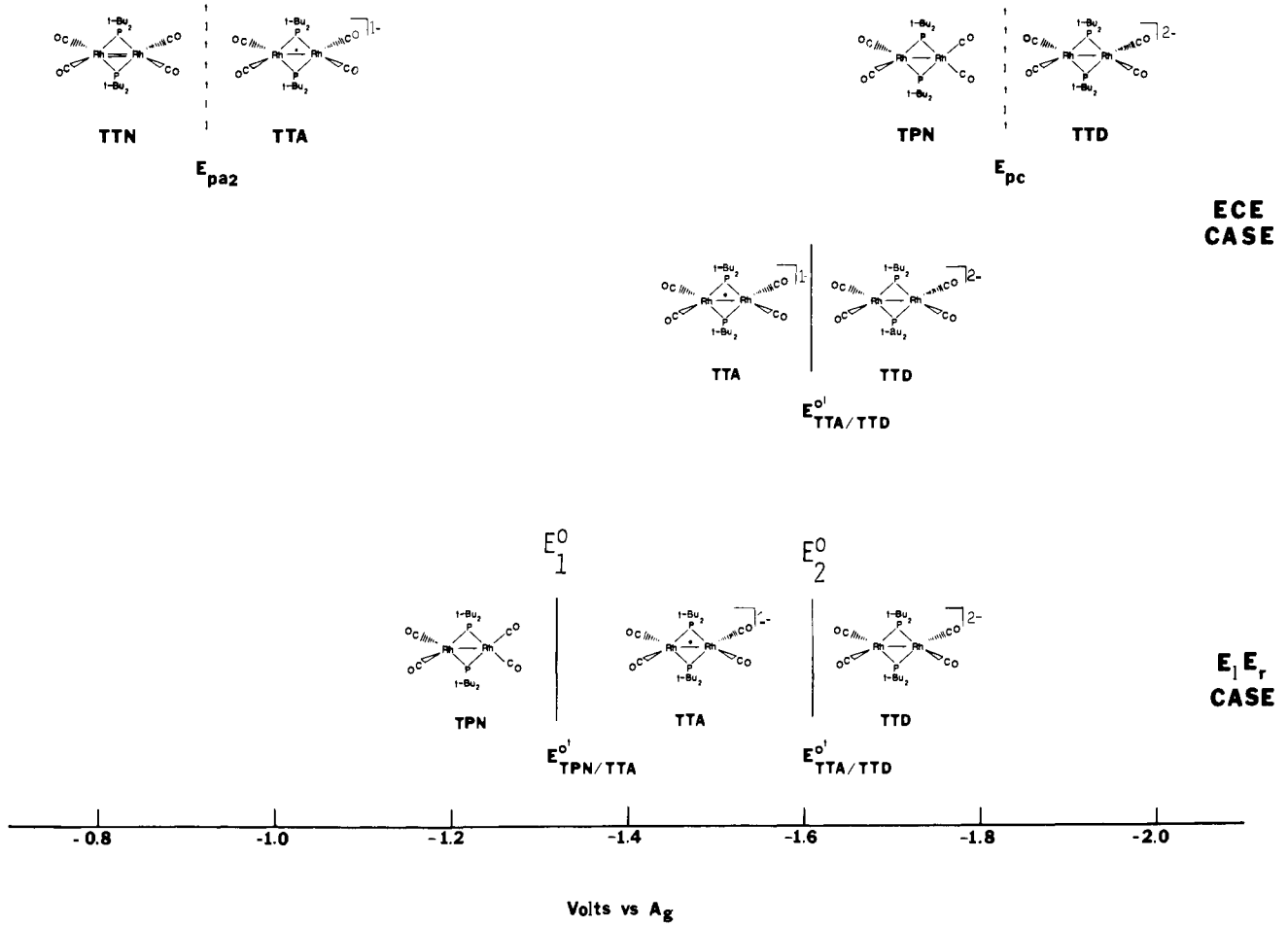

Figure 6. Summary of peak potentials and $E^{\circ\prime}$ values for the ECE/EEC-Disp and E_iE_r-Disp mechanisms. Peak potentials are those observed at 200 mV s^{-1}.

with $E^{\circ}_1 = E^{\circ\prime}_{TPN/TTA} = -1.34$ V and $E^{\circ}_2 = E^{\circ\prime}_{TTA/TTD} = -1.61$ V are given in Figure 5. The value of E°_1 was taken from E_{pc_1} and E_{pa_2} and an α_1 value of 0.45. Because the two cases are indistinguishable, the possibility of an E_iE_r mechanism cannot be ruled out on the basis of the observed voltammograms (compare Figures 3b, 4, and 5 with Figures 1 and 2b). However, the extremely small value needed for k°_1 in the simulations (9.6×10^{-7} cm s^{-1}) makes an E_iE_r-Disp mechanism unlikely and the ECE/EEC-Disp model is preferred.[28] Although it may at first appear that a large number of different combinations of k°_1 and E°_1 will yield the simulated voltammogram shown in Figure 5, once a value is chosen for α_1, only one combination of k°_1 and E°_1 will place the large reduction wave and the second oxidation wave at the correct potentials. The value of α_1 used in these simulations was chosen to give the best fit to the experimental voltammograms, since this parameter affects the current magnitude and wave shape. The experimental and simulated potentials for these models are summarized in Figure 6.

X-ray Crystal Structure and Spectroscopic Characterization of the Dianion $[Rh(\mu\text{-}t\text{-}Bu_2P)(CO)_2]_2^{2-}$ (*Rh-Rh*) (TTD) as Its n-Bu_4N^+ Salt. The electrochemically generated dianion $[Rh(\mu\text{-}t\text{-}Bu_2P)(CO)_2]_2^{2-}$ (TTD) may be isolated as its n-Bu_4N^+ salt by crystallization from THF. It is a bright red crystalline material which is air stable for short periods. Spectroscopic data for the dianion are consistent with the solid-state structure as determined by a single-crystal X-ray diffraction study. Thus, the IR spectrum (THF solution) shows two terminal ν_{CO} bands at 1760 (s) and 1733 cm^{-1} (s), consistent with D_{2h} symmetry. As expected the bands come to lower frequency than those observed for the neutral isomers (2038 (s), 1987 (s), 1952 cm^{-1} (s)). The $^{31}P\{^1H\}$ NMR spectrum shows a triplet to low field (δ 377.1, $^1J_{Rh-P} = 117$ Hz) consistent with the phosphido ligand bridging a metal–metal bond[28] and indicating that both rhodium atoms have the same geometry on the NMR time scale. The $^{13}C\{^1H\}$ NMR spectrum strongly indicates that the Rh atoms retain their pseudo-tetrahedral geometry in solution. The carbonyl carbon atoms (^{13}CO enriched) appear as a simple doublet to low field δ 218.0 (d, $^1J_{Rh-C} = 83.9$ Hz). The significant point about the data is that there is no coupling, or virtually zero coupling, to phosphorus. This is consistent with the carbonyl groups lying in a plane which is perpendicular to that which contains the central Rh_2P_2 core. A similar doublet signal with a remarkably similar $^1J_{Rh-C}$ coupling constant was observed in the low-temperature spectrum of $[Rh(\mu\text{-}t\text{-}Bu_2P)(CO)_2]_2$ (δ 202.5 (d, $^1J_{Rh-C} = 83.8$ Hz) and was also assigned to the carbonyls of the tetrahedral end of the molecule. The lack of $^2J_{P-C}$ coupling is no doubt due to different sets of metal orbitals being used to bond to the μ-t-Bu_2P and CO groups. A similar lack of (or very small) coupling between phosphorus has been

Table III. Bond Distances in Anstroms[a]

atom 1	atom 2	distance
Rh(1)	Rh(1′)	2.840 (1)
Rh(1)	P(1)	2.328 (2)
Rh(1)	P(1′)	2.316 (3)
Rh(1)	CO(1)	1.894 (12)
Rh(1)	CO(2)	1.875 (11)
P(1)	C(1)	1.880 (10)
P(1)	C(2)	1.918 (10)
OO(1)	CO(1)	1.152 (11)
OO(2)	CO(2)	1.146 (10)

[a] Numbers in parentheses are estimated standard deviations in the least significant digit.

(28) (a) Petersen, J. L.; Steward, R. P. *Inorg. Chem.* **1980**, *19*, 186–191. (b) Carty, A. *J. Adv. Chem. Ser.* **1982**, *No. 196*, 163. (c) Garrou, P. E. *Chem. Rev.* **1981**, *81*, 229–266.

Table IV. Bond Angles in Degrees[a]

atom 1	atom 2	atom 3	angle
Rh(1)	Rh(1')	P(1)	52.11 (6)
Rh(1)	Rh(1')	P(1')	52.48 (6)
Rh(1)	Rh(1')	CO(1)	122.8 (3)
Rh(1)	Rh(1')	CO(2)	119.6 (3)
P(1)	Rh(1)	P(1')	104.59 (8)
P(1)	Rh(1)	CO(1)	111.0 (3)
P(1)	Rh(1)	CO(2)	107.7 (3)
P(1)	Rh(1)	CO(1)	107.7 (3)
P(1)	Rh(1)	CO(2)	107.5 (3)
CO(1)	Rh(1)	CO(2)	117.5 (4)
Rh(1)	P(1)	Rh(1')	75.41 (8)
Rh(1)	P(1)	C(1)	117.1 (3)
Rh(1)	P(1)	C(2)	118.8 (3)
Rh(1)	P(1)	C(1')	121.1 (4)
Rh(1)	P(1)	C(2')	117.4 (4)
C(1)	P(1)	C(2)	105.5 (5)
Rh(1)	CO(1)	OO(1)	168.9 (8)
Rh(1)	CO(2)	OO(2)	168 (1)

[a] Numbers in parentheses are estimated standard deviations in the least significant digit.

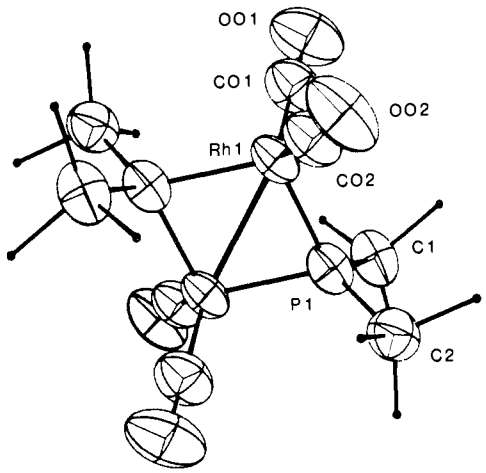

Figure 7. View of $[Rh(\mu\text{-}t\text{-}Bu_2P)(CO)_2]_2^{2-}$. Methyl groups on the *tert*-butyls have been reduced to sticks for clarity.

observed in the $^{31}P\{^1H\}$ spectra of phosphido-bridged complexes of the type $[M(\mu\text{-}R_2P)CO(PR_3)]_2$ (M = Co, Rh, Ir) in which the metals have pseudo-tetrahedral geometries and metal–metal bonds of order two.[11,15f,29]

X-ray Crystal Structure. Details of intensity data collection and structure refinement are given in Table I and the Experimental Section. Atomic positional parameters are given in Table II and bond lengths and bond angles are given in Tables III and IV, respectively. A view of the dianion is shown in Figure 7. The anion/cation packing in the unit cell is typical for complexes of this sort. Tables of anisotropic thermal parameters and structure factors are available as supplementary material.[30]

Molecules of the dianion possess a crystallographically imposed inversion center at the midpoint of the Rh–Rh vector. Thus, the central Rh_2P_2 core is rigorously planar. The Rh–Rh distance of 2.840 (1) Å falls within the range expected for a single Rh–Rh bond.[31] It is slightly longer than that found in the neutral tetrahedral/planar isomer, TPN (2.7609 (9) Å). The structural parameters for the rest of the dianion are similar to those of the tetrahedral end of the TPN isomer. Thus, the Rh(1)–P(1) and Rh(1)–CO(1) distances are 2.238 (2) and 1.894 (12) Å, respectively, compared to the analogous distances of 2.244 (2) and 1.88 (1) Å. The Rh(1)–P(1)–Rh(1') and CO(1)–Rh(1)–CO(2) angles for the dianion are 75.41 (8)° and 117.5 (4)° vs. analogus angles of 72.02 (7)° and 111.6 (4)° in the TPN isomer.

Conclusion

From our other studies of neutral Rh(I) dimers of type A, B, and C it is possible that relatively weak steric factors are finely balanced with electronic factors in determining the observed geometries. Thus, steric congestion around the metal results in pseudo-tetrahedral coordination for each formally 18-electron metal and a metal–metal double bond. When there is no steric strain in the system, the now formally 16-electron metals adopt a planar coordination geometry, presumably for electronic reasons;[32] no metal–metal interaction is required and none is observed.

Calculations have indicated that the three isomers A, B, and C are all extremely close in energy, and these results will be described separately.[33] For the $[Rh(\mu\text{-}t\text{-}Bu_2P)(CO)_2]_2$ system the square-planar/tetrahedral and square-planar/square-planar isomers are the ones which are actually observed, although the tetrahedral/tetrahedral form is no doubt very close in energy to them both. We assume that in the doubly bonded form (TTN) the metal–metal double bond consists of one σ and one π bond.

Why does the dinuclear system undergo geometric changes upon reduction and reoxidation? In the reduction process it seems reasonable to assume that the geometry of the system rearrages to place electrons in a molecular orbital of the lowest possible energy. Our observations, as well as theoretical calculations, suggest that this is a π^* antibonding orbital of the metal–metal doubly bonded isomer. In order to accommodate the two electrons upon reduction, the system is forced to rearrange to the tetrahedral/tetrahedral configuration. This, for the dianion, would result in a net Rh–Rh bond order of one, and this is consistent with the experimentally observed distance of 2.840 (1) Å. On reoxidation the system is permitted to rearrange to the more stable form involving a planar Rh(I) geometry.

Further studies are in progress.

Acknowledgements. We thank the Robert A. Welch Foundation and the National Science Foundation (CHE 82-11883 and CHE 7903729) for support. The X-ray diffractometer was purchased with funds from NSF (CHE 82-05871) and the University of Texas at Austin. We also thank Dr. John N. Ramsden for assistance in the preliminary stages of these investigations and Johnson-Matthey, Inc., for a generous loan of $RhCl_3 \cdot xH_2O$.

Appendix

The general reaction scheme (A, B, etc.) for the $[Rh(\mu\text{-}t\text{-}Bu_2P)(CO)_2]_2$ complex is

$$A + e^- \underset{k_{b1}}{\overset{k_{f1}}{\rightleftharpoons}} B \qquad (A.1)$$

$$B \xrightarrow{k_c} C \qquad (A.2)$$

$$C + e^- \underset{k_{b2}}{\overset{k_{f2}}{\rightleftharpoons}} D \qquad (A.3)$$

$$C \xrightarrow{k_{b3}} A + e^- \qquad (A.4)$$

The pertinent equations for the simulations are those that define the surface boundary conditions. The flux at the electrode surface ($x = 0$) is related to the current by

$$-\frac{i}{nFA} = f_{x=0} = D\left(\frac{\partial C}{\partial x}\right)_{x=0} \qquad (A.5)$$

where f is the flux, D is the diffusion coefficient, and C is the concentration. From the equations for the heterogeneous electron-transfer rate, the following surface boundary conditions are derived for the different species.

(29) Harley, A. D.; Whittle, R. R.; Geoffroy, G. L. *Organometallics* **1983**, *2*, 60–63.
(30) See paragraph at end of paper regarding supplementary material.
(31) Cowie, M.; Dwight, S. K. *Inorg. Chem.* **1980**, *19*, 209–216.
(32) Cotton, F. A.; Wilkinson, G "Advanced Inorganic Chemistry"; John Wiley and Sons, Inc.: New York, 1980; p 934.
(33) Kang, S. K.; Albright, T. A.; Wright, T. C.; Jones, R. A.; *Organometallics*, accepted for publication.

$$(f_A)_{x=0} = D_A\left(\frac{dC_A}{dx}\right)_{x=0} = k_{f1}C_A(x = 0) - k_{b1}C_B(x = 0) - k_{b3}C_C(x = 0) \quad (A.6)$$

$$(f_B)_{x=0} = D_B\left(\frac{dC_B}{dx}\right)_{x=0} = k_{b1}C_B(x = 0) - k_{f1}C_A(x = 0) \quad (A.7)$$

$$(f_C)_{x=0} = D_C\left(\frac{dC_C}{dx}\right)_{x=0} = f_{f2}C_C(x = 0) - k_{b2}C_D(x = 0) + k_{b3}C_C(x = 0) \quad (A.8)$$

$$(f_D)_{x=0} = D_D\left(\frac{dC_D}{dx}\right)_{x=0} = k_{b2}C_D(x = 0) - k_{f2}C_C(x = 0) \quad (A.9)$$

The flux that defines the current, the faradaic flux, is given by

$$f_{far} = k_{f1}C_A(x = 0) - k_{b1}C_B(x = 0) - k_{b3}C_C(x = 0) - k_{b2}C_D(x = 0) + k_{f2}C_C(x = 0) \quad (A.10)$$

$$f_{far} = (f_A)_{x=0} - (f_D)_{x=0} \quad (A.11)$$

In the notation for the finite-difference method of digital simulations,[20] eq A.6–A.10 become

$$(f_A)_{x=0} = \frac{2D_A[C_A(1) - C_A(0)]}{\Delta x} = k_{f1}C_A(0) - k_{b1}C_B(0) - k_{b3}C_C(0) \quad (A.12)$$

$$(f_B)_{x=0} = \frac{2D_B[C_B(1) - C_B(0)]}{\Delta x} = k_{b1}C_B(0) - k_{f1}C_A(0) \quad (A.13)$$

$$(f_C)_{x=0} = \frac{2D_C[C_C(1) - C_C(0)]}{\Delta x} = k_{f2}C_C(0) - k_{b2}C_D(0) + k_{b3}C_C(0) \quad (A.14)$$

$$(f_D)_{x=0} = \frac{2D_D[C_D(1) - C_D(0)]}{\Delta x} = k_{b2}C_D(0) - k_{f2}C_C(0) \quad (A.15)$$

$$f_{far} = k_{f1}C_A(0) - k_{b1}C_B(0) - k_{b3}C_C(0) - k_{b2}C_D(0) + k_{f2}C_C(0) \quad (A.16)$$

where for any species, j, $C_j(1)$ and $C_j(0)$ are the concentrations of species j in the first box and at the electrode surface, respectively. Δx is the width of a solution box. Solving for $C_j(0)$

$$C_j(0) = C_j(1) - \frac{\Delta x(f_j)_{x=0}}{2D_j} \quad (A.17)$$

eliminating $C_j(0)$ in the rate equations (eq A.12–A.15) and letting

$$\epsilon_0 = k_{f1}C_A(1) \qquad \zeta_0 = k_{b3}C_C(1)$$
$$\epsilon_1 = k_{f1}\Delta x/2D_A \qquad \zeta_1 = k_{b3}\Delta x/2D_C$$
$$\chi_0 = k_{b1}C_B(1) \qquad \tau_0 = k_{b2}C_D(1)$$
$$\chi_1 = k_{b1}\Delta x/2D_B \qquad \tau_1 = k_{b2}\Delta x/2D_D$$
$$\eta_0 = k_{f2}C_C(1)$$
$$\eta_1 = k_{f2}\Delta x/2D_C$$

gives the following equations.

$$(f_A)_{x=0} = (\epsilon_0 - \chi_0 - \zeta_0) - \epsilon_1(f_A)_{x=0} + \chi_1(f_B)_{x=0} + \zeta_1(f_C)_{x=0} \quad (A.18)$$

$$(f_B)_{x=0} = (\chi_0 - \epsilon_0) - \chi_1(f_B)_{x=0} + \epsilon_1(f_A)_{x=0} \quad (A.19)$$

$$(f_C)_{x=0} = (\eta_0 - \tau_0 + \zeta_0) - \eta_1(f_C)_{x=0} + \tau_1(f_D)_{x=0} - \zeta_1(f_C)_{x=0} \quad (A.20)$$

$$(f_D)_{x=0} = (\tau_0 - \eta_0) - \tau_1(f_D)_{x=0} + \eta_1(f_C)_{x=0} \quad (A.21)$$

The flux eq A.18–A.21 are now in a form where the only unknown parameters are f_j and $C_j(1)$ since k_{fj} and k_{bj} are potential-dependent rate constants calculated from the Butler–Volmer equations.[20] Introducing eq A.21 into eq A.20 and solving for $(f_C)_{x=0}$ yields

$$(f_C)_{x=0} = \frac{\eta_0 + \zeta_0 - \tau_0 + \tau_1\zeta_0}{1 + \eta_1 + \zeta_1 + \tau_1 + \tau_1\zeta_1} \quad (A.22)$$

Placing eq A.19 into eq A.18 and solving for $(f_B)_{x=0}$ yields

$$(f_B)_{x=0} = \frac{\chi_0 - \epsilon_0 - \zeta_0\epsilon_1}{\chi_1 + \epsilon_1 + 1} + \frac{\epsilon_1\zeta_1}{\chi_1 + \epsilon_1 + 1}(f_C)_{x=0} \quad (A.23)$$

By use of eq A.22 and A.23, eq A.19 and A.21 can be expressed as

$$(f_A)_{x=0} = \frac{\epsilon_0 - \chi_0}{\epsilon_1} + \frac{1 + \chi_1}{\epsilon_1}(f_B)_{x=0} \quad (A.24)$$

$$(f_D)_{x=0} = \frac{\tau_0 - \alpha_0}{1 + \tau_1} + \frac{\eta_1}{1 + \tau_1}(f_C)_{x=0} \quad (A.25)$$

By use of A.16, A.24, and A.25 the faradaic flux, and thus the current, can be calculated.

Registry No. TTN, 84454-21-7; $[Rh(\mu\text{-}t\text{-}Bu_2P)(CO)_2]_2(N(n\text{-}Bu)_4)_2$, 94042-35-0; $[Rh(\mu\text{-}t\text{-}Bu_2P)(CO)_2]_2^-$, 94042-36-1; $[Rh(\mu\text{-}t\text{-}Bu_2P)(CO)_2]_2$, 84623-35-8; Rh, 7440-16-6.

Supplementary Material Available: Tables of atomic thermal parameters and structure factors for **4** (31 pages). Ordering information is given on any current masthead page.